

Variational Monte Carlo approach to the SU(4) spin-orbital model on the triangular lattice

Chun Zhang¹, Hui-Ke Jin², and Yi Zhou^{1,3,4,*}

¹*Institute of Physics, Chinese Academy of Sciences, Beijing 100190, China*

²*Physics Department, TUM School of Natural Sciences, Technical University of Munich, 85748 Garching, Germany*

³*Kavli Institute for Theoretical Sciences, University of Chinese Academy of Sciences, Beijing 100190, China*

⁴*CAS Center for Excellence in Topological Quantum Computation, University of Chinese Academy of Sciences, Beijing 100190, China*



(Received 5 November 2023; accepted 20 February 2024; published 4 March 2024)

Previous investigations have suggested that the simplest spin-orbital model on the simplest frustrated lattice can host a nematic quantum spin-orbital liquid state. Namely, the orbital degeneracy of the SU(4) Kugel-Khomskii model tends to enhance quantum fluctuations and stabilize a quantum spin-orbital liquid exhibiting stripy features on the triangular lattice, as revealed by the state-of-the-art method of the density matrix renormalization group boosted by Gutzwiller projected wave functions. In this work, using the variational quantum Monte Carlo method, we study several spin-orbital liquid states, including a uniform π -flux state, three stripy states, and a plaquette state, on the $L \times L$ torus up to $L = 24$. It turns out that one of these stripy states, called the “stripe-II” state, is energetically favored. This ground state breaks the C_6 symmetry of the lattice, resulting in a reduced C_2 symmetry and doubled unit cells while preserving the SU(4) spin-orbital rotation symmetry. Such a nematic quantum spin-orbital liquid state can be characterized by a parton Fermi surface (FS) consisting of open orbits in the Brillouin zone, in contrast to the circular FS of the uniform π -flux state.

DOI: [10.1103/PhysRevB.109.125103](https://doi.org/10.1103/PhysRevB.109.125103)

I. INTRODUCTION

The search for quantum spin liquids (QSLs) is one of the central issues in modern condensed matter physics [1–7]. In the 1970s, Anderson proposed a disordered ground state for the spin-1/2 antiferromagnetic (AFM) Heisenberg model on the triangular lattice [1], namely, the simplest spin model on the simplest geometrically frustrated lattice, which revealed the age of QSLs and resonating valence-bond states. However, after extensive studies, the academic community has reached a consensus that the spin-1/2 AFM Heisenberg model on the triangular lattice hosts a 120° magnetically ordered ground state, contrary to Anderson’s original proposal [8–10]. This means that the smallest spin quantum $S = 1/2$, which gives rise to the strongest quantum spin fluctuations, is still insufficient to completely suppress the classical magnetic order on the triangular lattice if only the nearest-neighbor (NN) Heisenberg spin interaction $\vec{S}_i \cdot \vec{S}_j$ is considered. Therefore, one has to turn to other ways of enhancing quantum fluctuations to realize a QSL ground state on the simplest geometrically frustrated lattice.

In addition to (1) the small spin quanta S and (2) geometric frustration, there are several other ways to enhance quantum spin fluctuations [11]: (3) competing spin interactions involving NN anisotropic spin couplings (e.g., the anisotropic Ising couplings in the Kitaev honeycomb model [12]) and isotropic (or anisotropic) spin couplings on longer bonds, (4) charge fluctuations near a Mott transition leading to multiple-spin interactions, and (5) additional degeneracy due to orbital degrees of freedom. Thus, QSL states can be achieved by stronger geometric frustration [13–16] or by

increasing competition among mutual interactions [17–24]. In particular, orbital degeneracy [i.e., path 5 above] can significantly enhance quantum fluctuations [25]. For instance, in some transition metal oxides, spin and orbital degrees of freedom may play a symmetric role, resulting in an enlarged SU(4) symmetry rather than the $SU(2) \times SU(2)$ spin-orbital rotational symmetry. The SU(4) Kugel-Khomskii (KK) model is the minimal model used to describe such spin-orbital materials [26–33], in which the SU(4) symmetry can amplify quantum fluctuations and potentially stabilize a spin-orbital liquid ground state.

Much theoretical effort has been devoted to the study of quantum phases in SU(4) quantum magnets. As an example, the one-dimensional SU(4) KK model is found to be integrable and to possess gapless excitations [34,35]. These gapless excitations are well characterized by the low-energy effective theory, i.e., the $SU(4)_1$ Wess-Zumino-Witten (WZW) conformal field theory (CFT) [36–38]. The ground state of the SU(4) KK model on the two-leg ladder is also well known, which breaks the translational symmetry and forms an SU(4) singlet plaquette [39,40]. This SU(4) singlet plaquette state can even be an exact ground state on the ladder, as long as the extra interactions have been properly chosen and added to the model Hamiltonian [41]. Unlike one-dimensional (1D) and ladder models, two-dimensional (2D) models are less clear, despite extensive research. For instance, several complementary methods indicated that the ground state of the SU(4) KK model on the honeycomb lattice is a Dirac-type spin-orbital liquid [42–44]. For the square lattice, several candidate ground states have been proposed for the SU(4) KK model, such as the plaquette ordered state [27,45], the \mathbf{Z}_2 spin-orbital liquid [46], and the dimerized and SU(4) symmetry-breaking state [47].

*yizhou@iphy.ac.cn

Especially, the ground state of the SU(4) KK model on the triangular lattice was debated until very recently. In the early days, exact diagonalization (up to 16 sites) and the variational approach (up to 64 sites) suggested an SU(4) singlet plaquette liquid ground state on which simple types of long-range correlations are suppressed [48]. Recently, the combination study of the density matrix renormalization group (DMRG) calculation on cylinders (with a circumference up to $L_y = 4$) and field theory analysis proposed a gapless liquid state with an emergent parton Fermi surface (FS) in the 2D limit [49]. In contrast, another DMRG study [50] and a self-consistent mean-field theory [51] preferred a stripe-ordered ground state. Soon thereafter, using a state-of-the-art method, DMRG boosted by Gutzwiller projected wave functions [52], two of the authors and their collaborators revisited this model [53]. The latest work revealed a nematic quantum spin-orbital liquid state, a critical stripy state that preserves SU(4) symmetry but breaks translational symmetry by doubling the unit cell along one of two primitive vectors. It was shown that the central charge of each stripe is $c = 3$, which is in quantitative agreement with the SU(4)₁ WZW CFT. Moreover, it was found that the DMRG-obtained state can be well described by a “single” Gutzwiller projected wave function with an emergent parton FS that consists of open orbits in the reciprocal space and indicates the nematicity. Such a “unified” picture captures all the essential physics in both quasi-1D cylinders (with circumferences up to $L_y = 8$) and the 2D limit, although the former exhibits a strong finite-size effect and even-odd discrepancy [53]. Note that the newly proposed parton FS consists of open orbits in reciprocal space, which must undergo a Lifshitz transition from the originally proposed π -flux state, which has a closed parton FS [49].

In this work, we reexamine the SU(4) KK model on the triangular lattice by using the variational Monte Carlo (VMC) approach. The advantage of the VMC method is to reduce the impact of finite-size effects in 2D systems and to impose periodic boundary conditions (PBCs) in both directions. Thus, the previously proposed Gutzwiller projected wave function [53] can be carefully verified at large tori, up to a lattice size of 24×24 . To this end, we have proposed five types of spin-orbital liquid states: a uniform π -flux state, three stripy states, and a plaquette state. After extensive numerical efforts, we have gathered strong evidence pointing to a critical stripy ground state, as revealed by the Gutzwiller-boosted DMRG [53].

The rest of this paper is organized as follows. We revisit the SU(4) KK model in Sec. II to make it self-contained. Then five fermionic parton mean-field ansatzes are proposed in Sec. III. In Sec. IV, we search for the ground state with the help of VMC and the stochastic reconfiguration method. Section V is devoted to a summary.

II. MODEL AND SYMMETRIES

The SU(4) KK model Hamiltonian on the triangular lattice is defined as

$$H = \frac{1}{2} \sum_{\langle i,j \rangle} (4\vec{S}_i \cdot \vec{S}_j + 1)(4\vec{T}_i \cdot \vec{T}_j + 1), \quad (1a)$$

where $\langle i, j \rangle$ denotes an NN bond and \vec{S}_i (\vec{T}_i) is the $S = 1/2$ spin (orbital) vector at site i . These spin (orbital) vectors can be represented by introducing $\vec{S}_i = \frac{1}{2}\{\sigma_i^x, \sigma_i^y, \sigma_i^z\}$ ($\vec{T}_i = \frac{1}{2}\{\tau_i^x, \tau_i^y, \tau_i^z\}$), where $\sigma^{x,y,z}$ ($\tau^{x,y,z}$) are the standard Pauli matrices acting on the twofold spin (orbital) indices. It is easy to verify that the Hamiltonian H in Eq. (1) commutes with all 15 generators of the SU(4) Lie group, $\lambda^1, \lambda^2, \dots, \lambda^{15}$, which are linear combinations of $\{\vec{\sigma}, \vec{\tau}, \vec{\sigma} \otimes \vec{\tau}\}$. Therefore, the SU(4) symmetry is respected by the model Hamiltonian.

The SU(4) symmetry becomes more transparent from the point of view that the $2 \times 2 = 4$ spin-orbital degrees of freedom at each site can be treated as a pseudospin. To demonstrate this, we introduce a 15-dimensional vector $\vec{\lambda}_i \equiv \{\lambda_i^1, \lambda_i^2, \dots, \lambda_i^{15}\}$ whose components are 15 SU(4) generators. Then the model Hamiltonian can be rewritten in terms of $\vec{\lambda}_i$ as

$$H = \sum_{\langle i,j \rangle} \left(\vec{\lambda}_i \cdot \vec{\lambda}_j + \frac{1}{2} \right). \quad (1b)$$

Note that these generators λ_i^μ have been normalized with $\text{tr}(\lambda_i^\mu \lambda_j^\nu) = 2\delta_{ij}\delta_{\mu\nu}$ [54]. So the Hamiltonian in Eq. (1) can be interpreted as an SU(4) AFM Heisenberg model, which is invariant under the global SU(4) pseudospin-rotation symmetry.

In addition to the SU(4) symmetry, this model is also symmetric with respect to the spatial symmetries of the triangular lattice, including the lattice translation symmetries $T_{1,2}$, the mirror symmetry M , and the sixfold rotation symmetry C_6 . Furthermore, as a spin-orbital system, this model naturally preserves the time-reversal symmetry.

III. PARTON CONSTRUCTION AND MEAN-FIELD ANSATZES

In this section, we first use the Gutzwiller projection to construct a trial wave function for solving the Hamiltonian H in Eq. (1). Given a specific variational wave function $|\Psi_{\text{trial}}\rangle$, one can calculate the ground-state energy E ,

$$E = \frac{\langle \Psi_{\text{trial}} | H | \Psi_{\text{trial}} \rangle}{\langle \Psi_{\text{trial}} | \Psi_{\text{trial}} \rangle},$$

by using the standard Monte Carlo method. This trial wave function can then be optimized by minimizing the energy E .

To construct such a trial Gutzwiller projected state, we introduce four flavors of fermionic partons at each site i , $f_{i\alpha}^\dagger$, for $\alpha = 1, 2, 3, 4$ ($f_{i\alpha}$ are the annihilation operators), where α denotes the four pseudospin (spin-orbital) degrees of freedom mentioned above. The SU(4) pseudospin operators can now be expressed in terms of these fermionic partons as

$$\lambda_i^\mu = f_i^\dagger \lambda^\mu f_i, \quad \mu = 1, \dots, 15, \quad (2)$$

where $f_i \equiv (f_{i1}, f_{i2}, f_{i3}, f_{i4})^T$ is a four-component vector. Instead of four spin-orbital states, these four flavors of fermions will generate $2^4 = 16$ states in Fock space at each local site. To restore the physical Hilbert space, a single-occupancy constraint of $\sum_{\alpha=1}^4 f_{i\alpha}^\dagger f_{i\alpha} = 1$ was imposed on each site; e.g., the Gutzwiller projection was implemented.

In this parton representation in Eq. (2), the inner product of two pseudospins $\vec{\lambda}_i \cdot \vec{\lambda}_j$ can be written in terms of

four-fermion interactions:

$$\begin{aligned} \vec{\lambda}_i \cdot \vec{\lambda}_j = & -2 \sum_{\alpha, \beta=1}^4 \left(f_{i\alpha}^\dagger f_{j\alpha} f_{j\beta}^\dagger f_{i\beta} + \frac{1}{4} f_{i\alpha}^\dagger f_{i\alpha} f_{j\beta}^\dagger f_{j\beta} \right) \\ & + \sum_{\alpha=1}^4 (f_{i\alpha}^\dagger f_{i\alpha} + f_{j\alpha}^\dagger f_{j\alpha}). \end{aligned} \quad (3)$$

Here the identity $\vec{\lambda}_{ab} \cdot \vec{\lambda}_{cd} = 2\delta_{ad}\delta_{bc} - \frac{1}{2}\delta_{ab}\delta_{cd}$ is used. Thus, the model Hamiltonian H in Eq. (1) can be recast as follows:

$$H = \sum_{\langle ij \rangle} \left(- \sum_{\alpha, \beta=1}^4 f_{i\alpha}^\dagger f_{j\alpha} f_{j\beta}^\dagger f_{i\beta} + 1 \right). \quad (4)$$

Note that the single-occupancy condition was imposed in the derivation of the last equation. The four-fermion term can be decoupled by introducing the mean-field parameters on NN bonds $\langle ij \rangle$ as

$$\chi_{ij} = \chi_{ji}^* = \sum_{\alpha=1}^4 \langle f_{i\alpha}^\dagger f_{j\alpha} \rangle. \quad (5)$$

So we get a quadratic mean-field Hamiltonian

$$H_{\text{MF}} = \sum_{\langle ij \rangle} \sum_{\alpha=1}^4 \chi_{ij} f_{j\alpha}^\dagger f_{i\alpha} + \text{H.c.}, \quad (6)$$

which preserves the SU(4) symmetry and can be easily diagonalized now.

In fact, H_{MF} in Eq. (6) can be treated as a ‘‘variational Hamiltonian’’ or an ‘‘effective Hamiltonian’’ in which $\{\chi_{ij}\}$ is a set of variational parameters to be determined. Taking into account the single-occupancy constraint at the mean, i.e., $\sum_{\alpha=1}^4 \langle f_{i\alpha}^\dagger f_{i\alpha} \rangle = 1$, one can find a ground state $|\Psi_{\text{MF}}\rangle$ for the mean-field Hamiltonian H_{MF} at 1/4 filling. Then the trial wave function $|\Psi_{\text{trial}}\rangle$ can be constructed by performing the Gutzwiller projection on $|\Psi_{\text{MF}}\rangle$:

$$|\Psi_{\text{trial}}\rangle = P_G |\Psi_{\text{MF}}\rangle. \quad (7)$$

Here P_G is the Gutzwiller projector, which removes all components not singly occupied to locally enforce the single-occupancy constraint.

The set of parameters $\{\chi_{ij}\}$, together with the form of H_{MF} in Eq. (6), is called the ‘‘mean-field ansatz.’’ As long as a mean-field ansatz is given, one can evaluate the energy $E(\{\chi_{ij}\})$ by using the standard VMC method and minimize $E(\{\chi_{ij}\})$ to obtain an optimal set of parameters $\{\chi_{ij}\}$. Then, all the correlation functions can be computed with such an optimized wave function. It is worth mentioning that the mean-field parameters χ_{ij} can be determined up to an overall positive factor via the ground state energy optimization. In the remainder of this section, we discuss several typical examples of SU(4)-symmetric mean-field ansatzes which will be utilized to construct trial wave functions.

Uniform π -flux state. Two of the simplest mean-field ansatzes are uniform zero-flux or π -flux states. Since the latter always has a lower energy than the former, we will skip the higher-energy zero-flux state and discuss only the uniform π -flux state. The uniform π -flux state is governed by the

mean-field Hamiltonian as follows:

$$H_{\Delta=\pi} = -t \sum_{\alpha=1}^4 \sum_{\langle ij \rangle} (f_{i\alpha}^\dagger f_{j\alpha} + \text{H.c.}), \quad (8)$$

which is obtained by setting $\chi_{ij} = -t$ ($t > 0$) on all the NN bonds in Eq. (6). In each elementary triangle, χ_{ij} will pick up a π flux, which gives the name to the π -flux state proposed in Ref. [49]. The parton FS at 1/4 filling is plotted in Fig. 1(a), which is almost a circle.

As an instability of the uniform π -flux state, a ‘‘stripy state’’ was recently proposed [53]. The stripy state breaks the lattice translational symmetry by doubling the unit cell along a certain lattice vector direction. In this work, we consider a more generic class of valence-bond-crystal (VBC) states. These VBC states have an enlarged 2×2 unit cell, as illustrated in Fig. 2(a). One can obtain stripy states or the uniform π -flux state by restoring the lattice translational symmetry along one or two lattice vector directions.

Generic 2×2 VBC states. Since the coordination number is $z = 6$ on a triangular lattice, each unit cell in a 2×2 VBC state has $2 \times 2 \times 6/2 = 12$ NN bonds, as labeled by $n = 1, 2, \dots, 12$ in Fig. 2(b). Thus, a generic VBC state can be depicted by 12 mean-field parameters χ_{ij} within one unit cell as

$$\chi_{ij} = -t_n, \quad (9)$$

such that the corresponding mean-field Hamiltonian takes the form

$$H_{\text{VBC}} = - \sum_{\alpha=1}^4 \sum_{n=1}^{12} \sum_{\langle ij \rangle_n} t_n (f_{i\alpha}^\dagger f_{j\alpha} + \text{H.c.}), \quad (10)$$

where $\langle ij \rangle_n$ denotes a type- n NN bond, as shown in Fig. 2(b). As mentioned above, stripy states can be obtained by restoring the lattice translational symmetry along either the x or y direction.

C_2 -stripe states. From a symmetry point of view, a stripy state will break the lattice translational symmetry in one direction while preserving it in the other. The D_6 rotational symmetry of the lattice will be broken simultaneously. The resulting stripy state may or may not remain a reduced C_2 rotational symmetry of the original D_6 symmetry. In particular, we are interested in the stripy states exhibiting the C_2 rotational symmetry, dubbed ‘‘ C_2 -stripe states.’’

Without loss of generality, we focus on stripy states that break the translational symmetry only along the x direction (associated with symmetry generator T_x). The unit cell is 2×1 and consists of six NN bonds. Therefore, there are only two sublattices, e.g., $A = C$ and $B = D$ in Fig. 2(b). The 12 values of χ_{ij} , say, t_n ($n = 1, 2, \dots, 12$), defined according to the labeling in Fig. 2(b) are reduced to 6 values in such a 2×1 VBC state. Namely, the constraint $t_n = t_{n+6}$ ($n = 1, 2, 3, 4, 5, 6$) should be imposed on Eqs. (9) and (10). Introducing a lattice site labeling scheme,

$$i = (x_i, y_i) = x_i \hat{x} + y_i \hat{y},$$

we find that for a 2×1 stripy state, χ_{ij} must satisfy, on NN bonds,

$$\begin{aligned} \chi_{i, i+\hat{x}} &= -t_{1(4)}, & \chi_{i, i+\hat{y}} &= -t_{2(5)}, \\ \chi_{i, i+\hat{x}-\hat{y}} &= -t_{3(6)}, & i &\in A \text{ (B)}. \end{aligned}$$

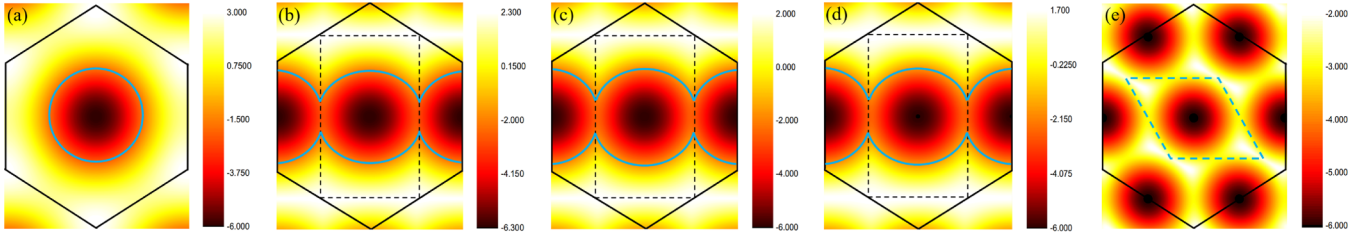


FIG. 1. The parton energy contour plot in the first (unfolded) Brillouin zone (BZ) for (a) the uniform π -flux state [Eq. (8)], (b) the stripe-I state [$\delta_1 = 0.15$ in Eq. (12)], (c) the stripe-II state [$\delta_1 = 0.15$ and $\epsilon = 0$ in Eq. (13)], (d) the stripe-III state [$\delta_1 = 0.15$ in Eq. (14)], and (e) the plaquette state [$\delta_1 = \delta_2 = 0.22$ in Eq. (15)], where the parameter $t = 1$ is set. The dashed lines in (b)–(e) enclose the folded BZ. At $1/4$ filling, (a) the uniform π -flux state has a closed Fermi surface (FS), and (b)–(d) stripe states allow an open FS in the BZ, while (e) the plaquette state is a parton band insulator.

Now we go further to consider C_2 -stripe states that respect the reduced C_2 rotational symmetry around the $\hat{x} - \frac{1}{2}\hat{y}$ axis, giving rise to $t_1 = t_3$ and $t_4 = t_6$. Therefore, the mean-field ansatz will take a simplified form on the six NN bonds in the 2×1 unit cell:

$$\chi_{i,i+\hat{x}} = \chi_{i,i+\hat{x}-\hat{y}} = -t_{1(4)}, \quad \chi_{i,i+\hat{y}} = -t_{2(5)}, \quad i \in A \text{ (B)}. \quad (11)$$

Note that due to symmetry there are only four different values of χ_{ij} , i.e., t_1, t_2, t_4 , and t_5 . Moreover, such a C_2 -stripe state is characterized by at most three independent parameters up to a positive total factor. In the following, we will discuss three types of C_2 -stripe states, called stripe-I, -II, and -III states, which were found by the VMC optimization to be local minima in the full parameter space for 2×2 VBC states, $\{t_1, t_2, \dots, t_{12}\}$.

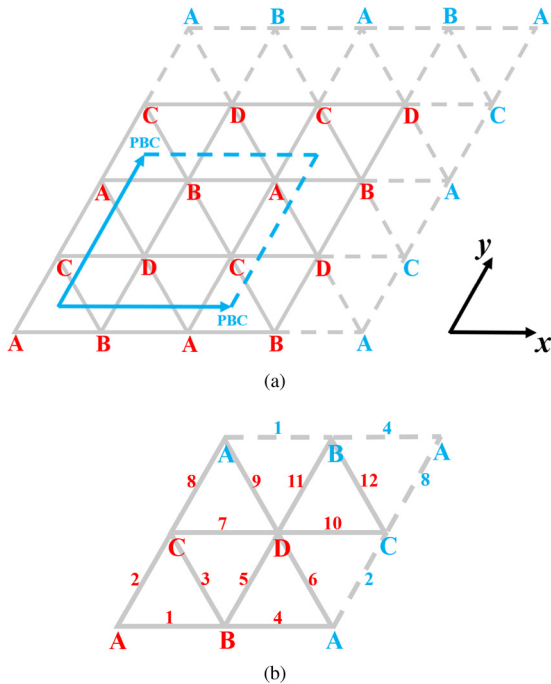


FIG. 2. For a 2×2 VBC on a triangular lattice, the unit cell has been enlarged to include four sublattices denoted by A, B, C, and D. (a) The XC torus geometry and the periodic boundary condition (PBC) are shown by dashed lines. (b) The 12 types of NN bonds in the enlarged unit cell.

Stripe-I state. This type of state can be achieved by setting

$$t_2 = t_4 = t_5 \quad (12a)$$

in Eq. (11). The mean-field ansatz for such a stripy state can be simplified as follows:

$$\chi_{ij} = -t(1 + r_{ij}\delta_1), \quad (12b)$$

where $r_{ij} = \pm 1$ is an integer defined by

$$r_{ij} = \delta_{x_i, x_j} + (-1)^{x_i}(1 - \delta_{x_i, x_j}), \quad (12c)$$

$t = (t_1 + t_4)/2$ serves as an overall factor, $\delta_1 = (t_4 - t_1)/(t_4 + t_1)$ is the contrast of the stripe, and $x_i \leq x_j$ is assumed for the NN bond $\langle ij \rangle$. Note that the stripe-I state is exactly equivalent to the trial wave function used to initialize the DMRG calculations in Ref. [53].

Stripe-II state. Imposing the constraint

$$t_2 = t_5 \quad (13a)$$

in Eq. (11) gives rise to the stripe-II state. The mean-field ansatz for such a state reads

$$\chi_{ij} = -t[1 + (-1)^{x_i}\delta_1](1 - \delta_{x_i, x_j}) - t(1 + \epsilon)\delta_{x_i, x_j}, \quad (13b)$$

where $t = (t_1 + t_4)/2$ is an overall factor, $\delta_1 = (t_4 - t_1)/(t_4 + t_1)$ reflects the stripe contrast, $\epsilon = t_2/t - 1$, and $x_i \leq x_j$ has been assumed for the NN bond $\langle ij \rangle$. When $\epsilon = \delta_1$, the stripe-II state becomes a stripe-I state.

Stripe-III state. Such a state can be achieved by setting

$$t_1 = t_2, \quad t_4 = t_5 \quad (14a)$$

in Eq. (11). The corresponding mean-field ansatz reads

$$\chi_{ij} = -t[1 + (-1)^{x_i}\delta_1], \quad (14b)$$

where $t = (t_1 + t_4)/2$, $\delta_1 = (t_4 - t_1)/(t_4 + t_1)$, and $x_i \leq x_j$ has been assumed for the NN bond $\langle ij \rangle$.

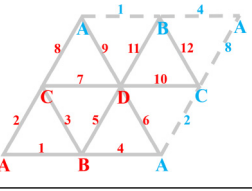
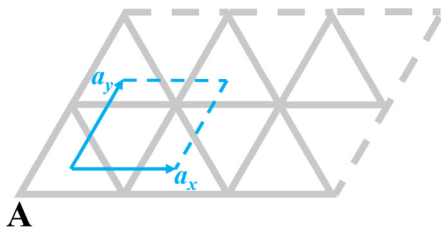
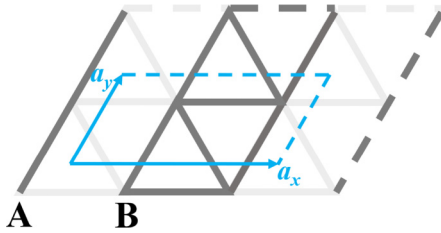
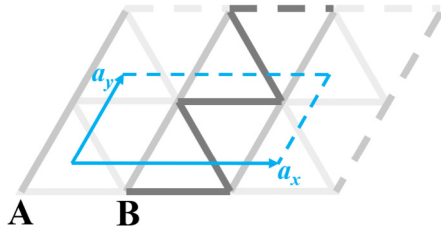
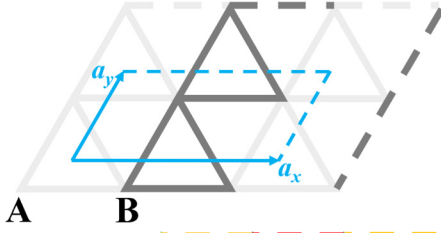
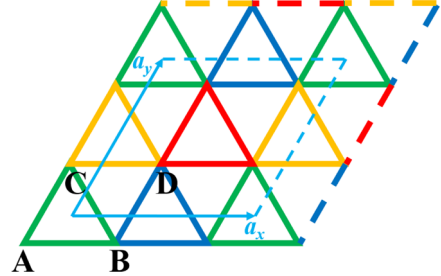
Plaquette state. In addition to the uniform π -flux state and the three C_2 -stripe states, we also consider the ‘‘plaquette state,’’ which is given by ‘‘perfect triangle conditions’’:

$$\begin{aligned} t_1 = t_2 = t_3, \quad t_4 = t_5 = t_6, \\ t_7 = t_8 = t_9, \quad t_{10} = t_{11} = t_{12} \end{aligned} \quad (15a)$$

and the constraint

$$t_1 + t_{10} = t_4 + t_7. \quad (15b)$$

TABLE I. Five types of mean-field ansatzes. Here $t_n > 0$ on all the NN bonds $(ij)_{n=1,\dots,12}$, suggesting that π -flux states are energetically favorable. T_x (T_y) shifts the system along the x (y) direction by a lattice constant.

	Schematic bond strength	Mean-field ansatz	Unit cell	Symmetry
				
Uniform π -flux state		$\chi_{ij} = -t$ [see Eq. (8)]	1×1	T_x, T_y, D_6
Stripe-I state		$t_{n+6} = t_n _{(n=1,\dots,6)}$, $t_2 = t_4 = t_5$ [see Eq. (12)]	2×1	T_x^2, T_y, C_2
Stripe-II state		$t_{n+6} = t_n _{(n=1,\dots,6)}$, $t_2 = t_5$ [see Eq. (13)]	2×1	T_x^2, T_y, C_2
Stripe-III state		$t_{n+6} = t_n _{(n=1,\dots,6)}$, $t_1 = t_2$, $t_4 = t_5$ [see Eq. (14)]	2×1	T_x^2, T_y, C_2
Plaquette state		$t_1 = t_2 = t_3$, $t_4 = t_5 = t_6$, $t_7 = t_8 = t_9$, $t_{10} = t_{11} = t_{12}$, $t_1 + t_{10} = t_4 + t_7$ [see Eq. (15)]	2×2	T_x^2, T_y^2

Thus, the mean-field ansatz for such a plaquette state takes the three-parameter form

$$\chi_{ij} = -t[1 + (-1)^{x_i} \delta_1 + (-1)^{\min\{y_i, y_j\}} \delta_2], \quad (15c)$$

where $x_i \leq x_j$ has been assumed for the NN bond (ij) , and the three parameters t , δ_1 , and δ_2 are determined by

$$\begin{aligned} t_1 + t_{10} = t_4 + t_7 = 2t, \quad t_1 = t(1 + \delta_1 + \delta_2), \\ t_4 = t(1 + \delta_1 - \delta_2). \end{aligned} \quad (15d)$$

It is worth noting that the parameter t for the five states that are defined in Eqs. (8), (12), (13), (14), and (15) can be unified as the average of the 12 t_n in Eq. (10),

$$t = \frac{1}{12} \sum_{n=1}^{12} t_n. \quad (16)$$

Before ending this section, we summarize five types of typical parton states in Table I, including (1) the uniform

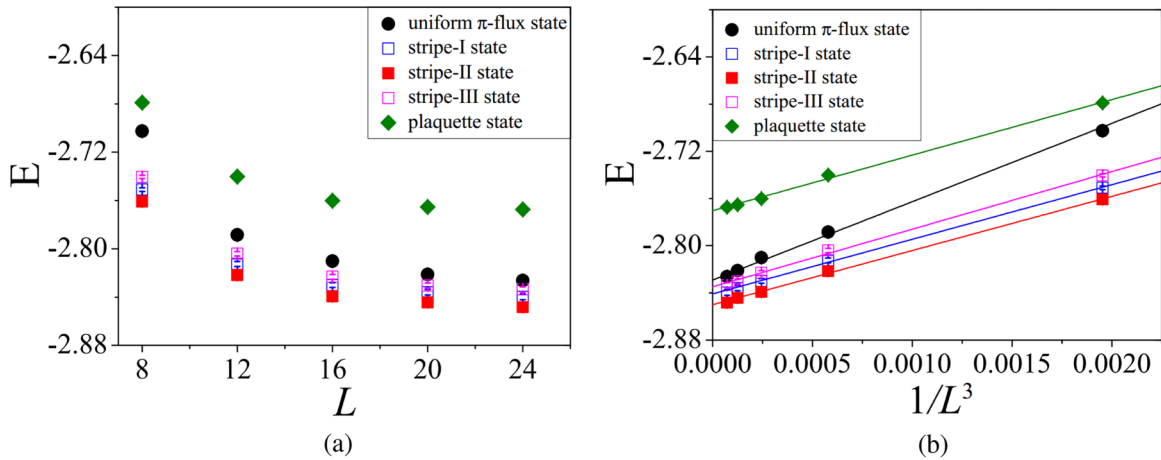


FIG. 3. All the local energy minima can be classified into the five types of states listed in Table I. (a) The optimized ground state energy for the five mean-field ansatzes listed in Table I. The lattice geometry is chosen to be an $L \times L$ XC torus with $L = 8, 12, 16, 20, 24$. (b) The linear fit of $E = E_\infty + \beta/L^3$, with $L = 8, 12, 16, 20, 24$. The values of E_∞ can be found in Table II. The energy error bar ($\sim 10^{-3}$) is approximately equal to the symbol size.

π -flux state, (2) the stripe-I state, (3) the stripe-II state, (4) the stripe-III state, and (5) the plaquette state. With $1/4$ parton filling, all stripy states allow an open parton FS when the stripe contrast exceeds a critical value, $\delta_1 > \delta_c$ (with $\delta_c \sim 0.1$), as shown in Fig. 1. However, the plaquette state is always a band insulator of fermionic partons.

IV. VMC CALCULATIONS AND RESULTS

We performed VMC calculations on various $L_x \times L_y$ XC lattices up to $L_x = L_y = 24$ [see definition of XC lattice in Fig. 2(a)], on which PBCs for SU(4) pseudospins were imposed along both the x and y directions. Thus, the parton boundary conditions can be either PBCs or antiperiodic boundary conditions (APBCs). Indeed, we found that the system always has a lower variational energy when the parton boundary conditions were chosen to be APBCs rather than PBCs along both the x and y directions.

First, we searched for local energy minima with generic 2×2 VBC states given in Eq. (10), parameterized by the set of $\{t_1, t_2, \dots, t_{12}\}$. To handle such a large parameter space, traditional methods such as steepest descent and Hessian matrix construction are computationally expensive and inefficient for optimizing the mean-field parameters. Therefore, a stochastic reconfiguration (SR) method was exploited to optimize the parameters [55,56]. In our calculations, a dynamic step length for the variational parameters t_n , ζ , was attempted during the VMC simulations, instead of a constant step length. At the beginning of optimization, a relatively large step length modulation, $\zeta \sim 5 \times 10^{-2}$, was chosen to avoid trapping E in local minima. Then we gradually decreased the modulation of ζ , and in the last 10^2 Monte Carlo steps, the step length was refined as $\zeta \sim 10^{-4}$. More details on the SR method can be found in Appendix A.

By performing extensive VMC computations initialized with a large number of sets of random $\{t_1, \dots, t_{12}\}$, we can draw two conclusions as follows:

Conclusion 1. All the energetically favorable states, found at local energy minima, correspond to a π -flux configuration, i.e., $t_n > 0$ for all $n = 1, \dots, 12$ in Eq. (9).

Conclusion 2. Within the numerical error bars, each local energy minimum found by the 12-parameter VMC optimizations can be identified as either the uniform π -flux state, one of the three C_2 stripy states, or a plaquette state (see Table I).

Based on these two results, we performed further VMC calculations on $L_x = L_y = L$ tori using the five promising parton mean-field ansatzes listed in Table I. Explicitly, in addition to the 12-parameter VMC approach, we also applied the parameter constraints defined in Eqs. (12), (13), (14), and (15) to our VMC calculations. Indeed, we found that all these simulations converge to energy minima that share the same energy with those obtained using the 12-parameter VMC optimization, supporting Conclusion 2. More details can be found in Appendix B. The main results are summarized in Fig. 3 and Table II. The optimized ground state energies are plotted as a function of the linear size L [see Fig. 3(a)] as well as its inverse cube $1/L^3$ [see Fig. 3(b)] [57–59]. Note that here the optimizations were done with the 12 variational parameters $t_{1,\dots,12}$ and all the local energy minima were classified into five types of states as listed in Table I. For all five types of local energy minima found in the 12 variational parameter optimization, the optimized ground state energy and corresponding mean-field parameters are given in Table II.

Using the formula $E(L) = E_\infty + \beta/L^3$ [57–59], extrapolation to the thermodynamic limit $L \rightarrow \infty$ allows us to draw a third conclusion:

Conclusion 3. Among all five types of ansatzes listed in Table I, the stripe-II state has the lowest ground state energy.

Stability of variational ground states. We will now investigate the energetic stability of these variational ground states. To do this, we introduce a Gaussian noise for a given mean-field ansatz $\{t_i\}$ such that $t_n \rightarrow t_n + \delta t_n$, where $\delta t_n \sim 0.01 t_n$ and the constraint $\sum_n \delta t_n = 0$ has been imposed. We then initialize the VMC computations with these noisy ansatzes and allow all 12 parameters $t_{n=1,\dots,12}$ to be optimized during the VMC computations.

We observe that the stripe-II state and the plaquette state are stable against noise in VMC simulations, even when a relatively strong Gaussian noise $\{\delta t_i\}$ is added. This means that

TABLE II. The optimized ground state energy and corresponding mean-field parameters for all five types of local energy minima found in the 12 variational parameter optimization. E_{24} is the optimized ground state energy on an XC(24×24) torus. E_∞ is obtained from the linear fit $E = E_\infty + \beta/L^3$, with $L = 8, 12, 16, 20, 24$. The variational parameters t_n ($n = 1, 2, \dots, 12$), δ_1 , δ_2 , and ϵ are defined in Eqs. (10), (11), (12), (13), and (14). Here we set the average $t = \frac{1}{12} \sum_{n=1}^{12} t_n$ as the unit of t_n [see Eq. (16)].

	E_{24}	E_∞	t_n	$\delta_1, \delta_2, \epsilon$
Uniform π -flux state	-2.8263 ± 0.0023	-2.8292 ± 0.0025	$t_n _{(n=1,\dots,12)} \approx t$ [see Eq. (8)]	
Stripe-I state	-2.8397 ± 0.0024	-2.8409 ± 0.0023	$t_1/t \approx 0.816, t_4/t \approx 1.092,$ $t_{n+6} \approx t_n _{(n=1,\dots,6)}, t = (t_1 + t_4)/2$ [see Eq. (12)]	$\delta_1 \approx 0.145$
Stripe-II state	-2.8484 ± 0.0026	-2.8500 ± 0.0026	$t_1/t \approx 0.849, t_4/t \approx 1.151,$ $t_2/t \approx 1.0, t_{n+6} \approx t_n _{(n=1,\dots,6)},$ $t = (t_1 + t_4)/2$ [see Eq. (13)]	$\delta_1 \approx 0.151 \approx \epsilon \approx 0$
Stripe-III state	-2.8335 ± 0.0022	-2.8349 ± 0.0028	$t_1/t \approx 0.854, t_4/t \approx 1.146,$ $t_{n+6} \approx t_n _{(n=1,\dots,6)}, t = (t_1 + t_4)/2$ [see Eq. (14)]	$\delta_1 \approx 0.146$
Plaquette state	-2.7673 ± 0.0023	-2.7703 ± 0.0026	$t_1/t \approx 0.58, t_4 \approx t_7 \approx t_2, t_{10}/t \approx 1.42,$ $t = (t_1 + t_{10})/2$ [see Eq. (15)]	$\delta_1 \approx \delta_2 \approx 0.210$

a noisy stripe-II state converges to a stripe-II state after VMC optimization, and so does a noisy plaquette state. In contrast, the uniform π -flux state, the stripe-I state, and the stripe-III state are inherently unstable to Gaussian noise. They easily converge to a stripe-II state instead of the original state type during VMC optimization.

Most stable ground state. We now discuss the most stable ground state, the stripe-II state defined in Eq. (13). First, we illustrate in Fig. 4 the set of all 12 variational parameters $\{t_1, t_2, \dots, t_{12}\}$ for the fully optimized state on an XC(24×24) torus. Note that such a state satisfies the constraints $t_{n+6} = t_n|_{n=1,\dots,6}$ and $t_2 = t_5$ within the error bar, which defines a

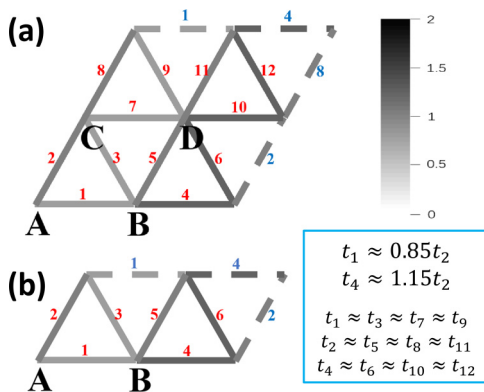


FIG. 4. Stripe-II state on an XC(24×24) torus. The lowest energy state is characterized by 12 variational parameters $t_{n=1,\dots,12}$, which are illustrated by a gray color map. (a) A large unit cell on the XC(24×24) torus for a 2×2 generic VBC state. The dashed lines indicate PBCs. (b) A unit cell for the stripe-II state. Here $t_1 + t_4 = 2t_2$ or $\epsilon = 0$ [defined in Eq. (13)] is found.

stripe-II state. Moreover, this stripe-II state reaches its lowest energy at $t_1 + t_4 = 2t_2$ or $\epsilon = 0$ in Eq. (13).

Second, we focus on the stripe-II state defined in Eq. (13), which is characterized by two independent parameters δ_1 and ϵ . Motivated by the above result of the stripe-II state during the 12-parameter optimization, we fix $\epsilon = 0$ and explore the ground state energy by varying δ_1 in Eq. (13). The ground state energy $E(\delta_1, \epsilon = 0)$ was calculated on an $L \times L$ torus and plotted in Fig. 5 as a function of δ_1 , considering different system sizes of $L = 8, 12, 16, 20, 24$. Remarkably, the minimum energy was found to be $E_{\min} = -2.8386 \pm 0.0027$ with $\delta_1 = 0.15$ on an $L = 24$ lattice, showing strong

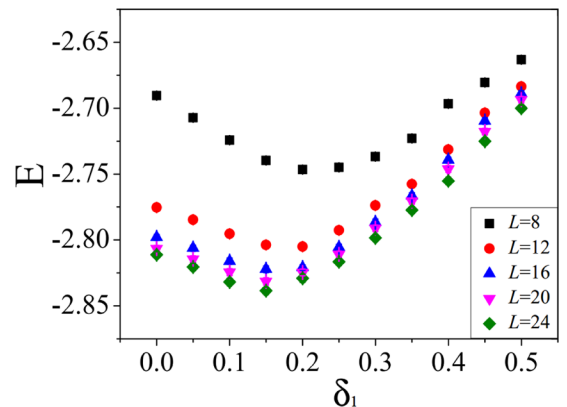


FIG. 5. Stripe-II states on an XC($L \times L$) torus. Here we set $\epsilon = 0$ in Eq. (13). The ground state energy $E(\delta_1, \epsilon = 0)$ is plotted as a function of δ_1 for $L = 8, 12, 16, 20, 24$. The energy error bar ($\sim 10^{-3}$) is approximately equal to the symbol size. The energy minimum is found to be $E_{\min} = -2.8386 \pm 0.0027$, with $\delta_1 = 0.15$ on the $L = 24$ lattice.

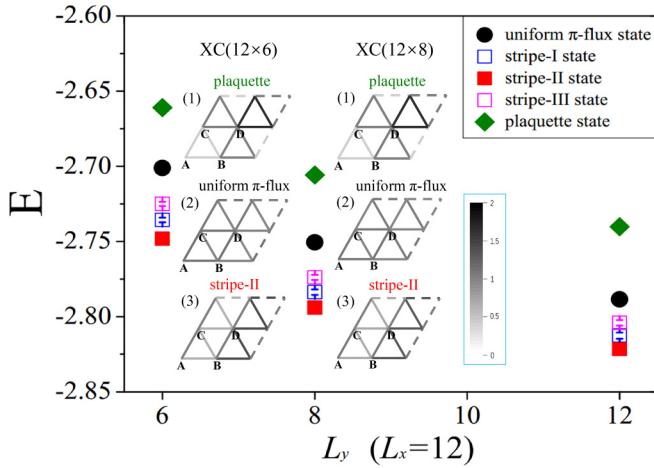


FIG. 6. The optimized energy $E(t_1, \dots, t_{12})$ for different shapes of $XC(L_x \times L_y)$ tori. Here $L_x = 12$ is fixed, and L_y is chosen to be $L_y = 6, 8, 12$. Insets 1, 2, and 3 represent three types of states in a gray color map. The energy error bar ($\sim 10^{-3}$) is approximately equal to the symbol size.

agreement with the results obtained with the 12-parameter optimization.

Finite-size effect. Finally, we would like to examine the finite-size effect on lattices with different aspect ratios L_x/L_y . To do this, we fix L_x and vary L_y and then perform VMC calculations on the $XC(L_x \times L_y)$ tori using the 12-parameter optimization. A number of typical results are shown in Fig. 6. We find that the stripe-II state remains the lowest energy state as the aspect ratio L_x/L_y varies; i.e., our conclusions remain unaffected by variations in the aspect ratio.

It is also interesting to consider how the chosen geometry affects the presence of stripy states. For instance, a potential avenue is the investigation of the torus geometry with twisted boundary conditions, which we leave for future studies.

V. SUMMARY

In summary, the VMC method was exploited to study the $SU(4)$ -symmetric spin-orbital model, i.e., the so-called Kugel-Khomskii model, on the triangular lattice. Beginning with a generic 2×2 valence-bond-crystal state that is characterized by 12 variational parameters $\{t_1, t_2, \dots, t_{12}\}$, we performed extensive VMC calculations and found that (1) all the local energy minima exhibit a π -flux configuration, (2) the optimized local energy minimum must belong to one of five types of states that include the uniform π -flux state, three C_2 -stripe states (dubbed the stripe-I, stripe-II, and stripe-III states), and the plaquette state, as listed in Table I, and (3) the stripe-II state has the lowest ground state energy with an extrapolated value of $E_\infty = -2.8500 \pm 0.0026$ in the thermodynamic limit.

This strip-II state breaks the lattice C_6 rotational symmetry to a C_2 rotational symmetry and has 2×1 unit cells. Since the $SU(4)$ spin-orbital rotational symmetry is respected, such a state is, indeed, a nematic quantum spin-orbital liquid state. The low energy excitations on top of the ground state are

gapless and can be represented by a parton Fermi surface consisting of open orbits in the Brillouin zone. All of these results are in excellent agreement with previous results obtained from the Gutzwiller-boosted DMRG [53].

ACKNOWLEDGMENTS

We would like to thank R.-Y. Sun and H.-H. Tu for their helpful discussions. This work is supported in part by the National Key Research and Development Program of China (Grant No. 2022YFA1403403), the National Natural Science Foundation of China (Grants No. 12274441 and No. 12034004), and the European Research Council (ERC) under the European Union's Horizon 2020 research and innovation program (Grant Agreement No. 771537).

APPENDIX A: STOCHASTIC RECONFIGURATION METHOD IN VMC CALCULATIONS

To perform the variational Monte Carlo (VMC) optimization, a stochastic reconfiguration (SR) method is adopted. It simulates the effect of the Hessian matrix with a more cost-effective approach, which we now review briefly.

When carrying out the VMC optimization, one key step is the computation of the expectation value of the Hamiltonian and its gradient with respect to the variational parameters. Without loss of generality, the variational state $|\Psi\rangle$ can be constructed by the wave function $|\Psi(C)\rangle$ in an orthonormal basis $|C\rangle$, written as

$$|\Psi\rangle = \sum_C \Psi(C)|C\rangle. \quad (\text{A1})$$

Then, the variational energy is given by

$$E = \frac{\langle \Psi | H | \Psi \rangle}{\langle \Psi | \Psi \rangle} = \frac{\sum_C |\Psi(C)|^2 E_{\text{loc}}(C)}{\sum_C |\Psi(C)|^2}. \quad (\text{A2})$$

The local energy E_{loc} is sampled, and its average value is calculated by

$$E_{\text{loc}}(C) = \sum_{C'} \frac{\langle C | H | C' \rangle \Psi(C')}{\Psi(C)}. \quad (\text{A3})$$

When searching for the minimum energy of $E(t_1, \dots, t_{12})$, a value taking the condition $\sum_{n=1}^{12} t_n = 12$ is imposed. For convenience, the series of parameters in the wave function $|\Psi(t_1, t_2, \dots, t_{12})\rangle$ are abbreviated as $\{\theta\}$. The gradient of the variational energy with respect to the variational parameters $\{\theta\}$ is given by

$$\begin{aligned} \nabla_\theta E(\theta) = & 2 \langle \nabla_\theta [\ln \Psi(C)] E_{\text{loc}}(C) \rangle \\ & - 2 \langle E_{\text{loc}}(C) \rangle \langle \nabla_\theta [\ln \Psi(C)] \rangle, \end{aligned} \quad (\text{A4})$$

which is obtained by the derivative with respect to $\{\theta\}$ of the following formula:

$$E(\theta) = \frac{\langle \Psi(\theta) | H | \Psi(\theta) \rangle}{\langle \Psi(\theta) | \Psi(\theta) \rangle}. \quad (\text{A5})$$

In formula (A4), the two quantities can be calculated using standard Monte Carlo sampling on the distribution generated by $|\Psi(\theta)|^2$, and the quantity $\langle \nabla_\theta (\ln \Psi(C)) \rangle$ will play a key role in the calculation of the gradient.

TABLE III. The optimized ground states for four types of Gutzwiller projected states listed in Table I. Here E_L is the optimized ground state energy per site on an XC($L \times L$) torus with $L = 12, 16, 24$. The variational parameters δ_1 , δ_2 , and ϵ are defined in Eqs. (10), (11), (12), (13), and (14).

	$L = 12$		$L = 16$		$L = 24$	
	E_L	$\delta_1, \delta_2, \epsilon$	E_L	$\delta_1, \delta_2, \epsilon$	E_L	$\delta_1, \delta_2, \epsilon$
Stripe-I state	-2.8091 ± 0.0014	$\delta_1 \approx 0.174$	-2.8276 ± 0.0021	$\delta_1 \approx 0.156$	-2.8377 ± 0.0024	$\delta_1 \approx 0.145$
Stripe-II state	-2.8174 ± 0.0015	$\delta_1 \approx 0.181 \epsilon \approx 0$	-2.8369 ± 0.0021	$\delta_1 \approx 0.161 \epsilon \approx 0$	-2.8462 ± 0.0024	$\delta_1 \approx 0.151 \epsilon \approx 0$
Stripe-III state	-2.8015 ± 0.0014	$\delta_1 \approx 0.177$	-2.8210 ± 0.0020	$\delta_1 \approx 0.156$	-2.8312 ± 0.0025	$\delta_1 \approx 0.145$
Plaquette state	-2.7401 ± 0.0010	$\delta_1 \approx 0.218 \delta_2 \approx 0.217$	-2.7600 ± 0.0018	$\delta_1 \approx \delta_2 \approx 0.203$	-2.7670 ± 0.0020	$\delta_1 \approx \delta_2 \approx 0.208$

To obtain the adjustment direction and the step length of $\{\theta\}$, an approximate Hessian matrix $\langle \Psi(\theta) | H | \dot{\Psi}(\theta) \rangle$ requires the construction

$$\frac{\partial^2}{\partial \theta \partial \theta'} \frac{\langle \Psi(\theta) | \Psi(\theta') \rangle}{\langle \Psi(\theta) | \Psi(\theta) \rangle}. \quad (\text{A6})$$

As the essence of the SR method, the second derivative of the energy with respect to parameters $\{\theta\}$ can be obtained with matrix (A6). To imitate the effect of the Hessian matrix, a positive-definite Hermitian matrix S generated from the metric of the variational state in the variational space is proposed. More specifically, the matrix element is given by

$$S_{ij} = \langle \nabla_{\theta} [\ln \Psi(C)]_i | \nabla_{\theta} [\ln \Psi(C)]_j \rangle - \langle \nabla_{\theta} [\ln \Psi(C)]_i | \nabla_{\theta} [\ln \Psi(C)]_j \rangle, \quad (\text{A7})$$

where the index i is with respect to the i th variational parameter.

Thanks to the quantity $\langle \nabla_{\theta} [\ln \Psi(C)] \rangle$ derived from Eq. (A4), an approximate Hessian matrix S can be obtained from Eq. (A7). Therefore, the direction and step length for performing parameter optimization can be found as follows:

$$\Delta \vec{\theta} = -\frac{1}{2\kappa} S^{-1} \vec{g}. \quad (\text{A8})$$

Here κ is an empirical positive parameter which is adjusted manually and defines the step length of the parameter optimization.

APPENDIX B: VMC CALCULATIONS FOR FOUR GUTZWILLER PROJECTED STATES LISTED IN TABLE I

In the main text, using the SR method, we searched for local energy minima on XC($L \times L$) tori up to $L = 24$ (see Fig. 3 and Table II) with the generic 12-parameter 2×2 VBC states given in Eq. (10). In this Appendix, we perform standard VMC calculations and search for local energy minima for four Gutzwiller projected states on XC($L \times L$) tori with $L = 12, 16, 24$. These Gutzwiller projected states are characterized by one or two variational parameters, as listed in Table I, namely, δ_1 in Eqs. (12) and (14) (stripe-I and stripe-III states), δ_1 and ϵ in Eq. (13) (stripe-II state), and δ_1 and δ_2 in Eq. (15) (plaquette state).

The optimized ground state energy and corresponding variational parameters are given in Table III and are consistent with the 12-parameter optimization results shown in Table II and Fig. 3 in the main text.

- [1] P. Anderson, Resonating valence bonds: A new kind of insulator? *Mater. Res. Bull.* **8**, 153 (1973).
- [2] P. A. Lee, An end to the drought of quantum spin liquids, *Science* **321**, 1306 (2008).
- [3] L. Balents, Spin liquids in frustrated magnets, *Nature (London)* **464**, 199 (2010).
- [4] Y. Zhou, K. Kanoda, and T.-K. Ng, Quantum spin liquid states, *Rev. Mod. Phys.* **89**, 025003 (2017).
- [5] L. Savary and L. Balents, Quantum spin liquids: A review, *Rep. Prog. Phys.* **80**, 016502 (2017).
- [6] J. Knolle and R. Moessner, A field guide to spin liquids, *Annu. Rev. Condens. Matter Phys.* **10**, 451 (2019).
- [7] C. Broholm, R. J. Cava, S. A. Kivelson, D. G. Nocera, M. R. Norman, and T. Senthil, Quantum spin liquids, *Science* **367**, eaay0668 (2020).
- [8] D. A. Huse and V. Elser, Simple variational wave functions for two-dimensional Heisenberg spin-1/2 antiferromagnets, *Phys. Rev. Lett.* **60**, 2531 (1988).
- [9] T. Jolicoeur and J. C. Le Guillou, Spin-wave results for the triangular Heisenberg antiferromagnet, *Phys. Rev. B* **40**, 2727 (1989).
- [10] S. R. White and A. L. Chernyshev, Neel order in square and triangular lattice Heisenberg models, *Phys. Rev. Lett.* **99**, 127004 (2007).
- [11] H.-K. Jin and Y. Zhou, Material search for quantum spin liquids on the simplest frustrated lattice, *Chin. Phys. Lett.* **39**, 050102 (2022).
- [12] A. Kitaev, Anyons in an exactly solved model and beyond, *Ann. Phys. (NY)* **321**, 2 (2006).
- [13] S. Yan, D. A. Huse, and S. R. White, Spin-liquid ground state of the $S = 1/2$ kagome Heisenberg antiferromagnet, *Science* **332**, 1173 (2011).
- [14] S. Depenbrock, I. P. McCulloch, and U. Schollwöck, Nature of the spin-liquid ground state of the $S = 1/2$ Heisenberg model on the kagome lattice, *Phys. Rev. Lett.* **109**, 067201 (2012).
- [15] H. J. Liao, Z. Y. Xie, J. Chen, Z. Y. Liu, H. D. Xie, R. Z. Huang, B. Normand, and T. Xiang, Gapless spin-liquid ground state in the $S = 1/2$ kagome antiferromagnet, *Phys. Rev. Lett.* **118**, 137202 (2017).
- [16] Y.-C. He, M. P. Zaletel, M. Oshikawa, and F. Pollmann, Signatures of Dirac cones in a DMRG study of the kagome Heisenberg model, *Phys. Rev. X* **7**, 031020 (2017).

- [17] M. S. Block, D. N. Sheng, O. I. Motrunich, and M. P. A. Fisher, Spin Bose-metal and valence bond solid phases in a spin-1/2 model with ring exchanges on a four-leg triangular ladder, *Phys. Rev. Lett.* **106**, 157202 (2011).
- [18] R. V. Mishmash, J. R. Garrison, S. Bieri, and C. Xu, Theory of a competitive spin liquid state for weak Mott insulators on the triangular lattice, *Phys. Rev. Lett.* **111**, 157203 (2013).
- [19] Z. Zhu and S. R. White, Spin liquid phase of the $S = \frac{1}{2} J_1 - J_2$ Heisenberg model on the triangular lattice, *Phys. Rev. B* **92**, 041105(R) (2015).
- [20] W.-J. Hu, S.-S. Gong, W. Zhu, and D. N. Sheng, Competing spin-liquid states in the spin- $\frac{1}{2}$ Heisenberg model on the triangular lattice, *Phys. Rev. B* **92**, 140403(R) (2015).
- [21] A. Wietek and A. M. Läuchli, Chiral spin liquid and quantum criticality in extended $S = \frac{1}{2}$ Heisenberg models on the triangular lattice, *Phys. Rev. B* **95**, 035141 (2017).
- [22] S.-S. Gong, W. Zhu, J.-X. Zhu, D. N. Sheng, and K. Yang, Global phase diagram and quantum spin liquids in a spin- $\frac{1}{2}$ triangular antiferromagnet, *Phys. Rev. B* **96**, 075116 (2017).
- [23] S. N. Saadatmand and I. P. McCulloch, Detection and characterization of symmetry-broken long-range orders in the spin- $\frac{1}{2}$ triangular Heisenberg model, *Phys. Rev. B* **96**, 075117 (2017).
- [24] S. Hu, W. Zhu, S. Eggert, and Y.-C. He, Dirac spin liquid on the spin-1/2 triangular Heisenberg antiferromagnet, *Phys. Rev. Lett.* **123**, 207203 (2019).
- [25] L. F. Feiner, A. M. Oleś, and J. Zaanen, Quantum melting of magnetic order due to orbital fluctuations, *Phys. Rev. Lett.* **78**, 2799 (1997).
- [26] K. I. Kugel and D. I. Khomskii, The Jahn-Teller effect and magnetism: transition metal compounds, *Sov. Phys. Usp.* **25**, 231 (1982).
- [27] Y. Q. Li, M. Ma, D. N. Shi, and F. C. Zhang, SU(4) theory for spin systems with orbital degeneracy, *Phys. Rev. Lett.* **81**, 3527 (1998).
- [28] S. K. Pati, R. R. P. Singh, and D. I. Khomskii, Alternating spin and orbital dimerization and spin-gap formation in coupled spin-orbital systems, *Phys. Rev. Lett.* **81**, 5406 (1998).
- [29] G. Khaliullin and S. Maekawa, Orbital liquid in three-dimensional Mott insulator: LaTiO₃, *Phys. Rev. Lett.* **85**, 3950 (2000).
- [30] Y. Tokura and N. Nagaosa, Orbital physics in transition-metal oxides, *Science* **288**, 462 (2000).
- [31] F. Reynaud, D. Mertz, F. Celestini, J.-M. Debierre, A. M. Ghorayeb, P. Simon, A. Stepanov, J. Voiron, and C. Delmas, Orbital frustration at the origin of the magnetic behavior in LiNiO₂, *Phys. Rev. Lett.* **86**, 3638 (2001).
- [32] M. G. Yamada, M. Oshikawa, and G. Jackeli, Emergent SU(4) symmetry in α -ZrCl₃ and crystalline spin-orbital liquids, *Phys. Rev. Lett.* **121**, 097201 (2018).
- [33] M. G. Yamada, M. Oshikawa, and G. Jackeli, SU(4)-symmetric quantum spin-orbital liquids on various lattices, *Phys. Rev. B* **104**, 224436 (2021).
- [34] B. Sutherland, Model for a multicomponent quantum system, *Phys. Rev. B* **12**, 3795 (1975).
- [35] Y.-Q. Li, M. Ma, D.-N. Shi, and F.-C. Zhang, Ground state and excitations of a spin chain with orbital degeneracy, *Phys. Rev. B* **60**, 12781 (1999).
- [36] I. Affleck, Exact critical exponents for quantum spin chains, non-linear σ -models at $\theta = \pi$ and the quantum Hall effect, *Nucl. Phys. B* **265**, 409 (1986).
- [37] P. Azaria, A. O. Gogolin, P. Lecheminant, and A. A. Nersisyan, One-dimensional SU(4) spin-orbital model: A low-energy effective theory, *Phys. Rev. Lett.* **83**, 624 (1999).
- [38] M. Fühlinger, S. Rachel, R. Thomale, M. Greiter, and P. Schmitteckert, DMRG studies of critical SU(N) spin chains, *Ann. Phys.* **520**, 922 (2008).
- [39] M. van den Bossche, P. Azaria, P. Lecheminant, and F. Mila, Spontaneous plaquette formation in the SU(4) spin-orbital ladder, *Phys. Rev. Lett.* **86**, 4124 (2001).
- [40] A. Weichselbaum, S. Capponi, P. Lecheminant, A. M. Tsvelik, and A. M. Läuchli, Unified phase diagram of antiferromagnetic SU(N) spin ladders, *Phys. Rev. B* **98**, 085104 (2018).
- [41] S. Chen, C. Wu, S.-C. Zhang, and Y. Wang, Exact spontaneous plaquette ground states for high-spin ladder models, *Phys. Rev. B* **72**, 214428 (2005).
- [42] P. Corboz, M. Lajkó, A. M. Läuchli, K. Penc, and F. Mila, Spin-orbital quantum liquid on the honeycomb lattice, *Phys. Rev. X* **2**, 041013 (2012).
- [43] W. M. H. Natori, R. Nutakki, R. G. Pereira, and E. C. Andrade, SU(4) Heisenberg model on the honeycomb lattice with exchange-frustrated perturbations: Implications for twistronics and Mott insulators, *Phys. Rev. B* **100**, 205131 (2019).
- [44] H.-K. Jin, W. M. H. Natori, and J. Knolle, Twisting the Dirac cones of the SU(4) spin-orbital liquid on the honeycomb lattice, *Phys. Rev. B* **107**, L180401 (2023).
- [45] M. van den Bossche, F. C. Zhang, and F. Mila, Plaquette ground state in the two-dimensional SU(4) spin-orbital model, *Eur. Phys. J. B* **17**, 367 (2000).
- [46] F. Wang and A. Vishwanath, Z₂ spin-orbital liquid state in the square lattice Kugel-Khomskii model, *Phys. Rev. B* **80**, 064413 (2009).
- [47] P. Corboz, A. M. Läuchli, K. Penc, M. Troyer, and F. Mila, Simultaneous dimerization and SU(4) symmetry breaking of 4-color fermions on the square lattice, *Phys. Rev. Lett.* **107**, 215301 (2011).
- [48] K. Penc, M. Mambrini, P. Fazekas, and F. Mila, Quantum phase transition in the SU(4) spin-orbital model on the triangular lattice, *Phys. Rev. B* **68**, 012408 (2003).
- [49] A. Keselman, B. Bauer, C. Xu, and C.-M. Jian, Emergent Fermi surface in a triangular-lattice SU(4) quantum antiferromagnet, *Phys. Rev. Lett.* **125**, 117202 (2020).
- [50] Y.-H. Zhang, D. N. Sheng, and A. Vishwanath, SU(4) chiral spin liquid, exciton supersolid, and electric detection in Moiré bilayers, *Phys. Rev. Lett.* **127**, 247701 (2021).
- [51] X.-P. Yao, Y. Gao, and G. Chen, Topological chiral spin liquids and competing states in triangular lattice SU(N) Mott insulators, *Phys. Rev. Res.* **3**, 023138 (2021).
- [52] H.-K. Jin, H.-H. Tu, and Y. Zhou, Density matrix renormalization group boosted by Gutzwiller projected wave functions, *Phys. Rev. B* **104**, L020409 (2021).
- [53] H.-K. Jin, R.-Y. Sun, H.-H. Tu, and Y. Zhou, Unveiling a critical stripy state in the triangular-lattice SU(4) spin-orbital model, *Sci. Bull.* **67**, 918 (2022).

- [54] H. Georgi, *Lie Algebras in Particle Physics* (Westview Press in Perseus Books, Boulder, Colorado, USA, 1999).
- [55] S. Sorella, Green function Monte Carlo with stochastic reconfiguration, *Phys. Rev. Lett.* **80**, 4558 (1998).
- [56] S. Sorella and L. Capriotti, Green function Monte Carlo with stochastic reconfiguration: An effective remedy for the sign problem, *Phys. Rev. B* **61**, 2599 (2000).
- [57] E. Manousakis, The spin-1/2 Heisenberg antiferromagnet on a square lattice and its application to the cuprous oxides, *Rev. Mod. Phys.* **63**, 1 (1991).
- [58] M. Gross, E. Sánchez-Velasco, and E. Siggia, Ground-state properties of the two-dimensional antiferromagnetic Heisenberg model, *Phys. Rev. B* **39**, 2484 (1989).
- [59] H. Neuberger and T. Ziman, Finite-size effects in Heisenberg antiferromagnets, *Phys. Rev. B* **39**, 2608 (1989).